Applied Surface Science 533 (2020) 147471

Contents lists available at ScienceDirect

Applied Surface Science

journal homepage: www.elsevier.com/locate/apsusc

Surface segregation in Cr-Mn-Fe-Co-Ni high entropy alloys

Alberto Ferrari[a,b,*], Fritz Körmann[b,c]

[a] RUB Research School, Ruhr Universität Bochum, 44801 Bochum, Germany
[b] Materials Science and Engineering, Delft University of Technology, 2628CD Delft, the Netherlands
[c] Max-Planck-Institut für Eisenforschung GmbH, 40237 Düsseldorf, Germany

ARTICLE INFO

Keywords:
High entropy alloys
Surface segregation
Cantor alloy
CrMnFeCoNi

ABSTRACT

The reactivity of the surface of multicomponent metals such as High Entropy Alloys (HEAs) is rapidly gaining importance for corrosion and catalytic applications, but the mechanisms of surface segregation in these complex materials are poorly understood. Here we investigate with *ab initio* calculations the segregation thermodynamics in the magnetic Cr-Mn-Fe-Co-Ni HEA in vacuum, in the presence of O at the surface, and in the oxide phase. We predict a weak segregation of Ni for Cr-, Mn-, and Fe-rich alloys in vacuum and a very strong segregation of Cr and Mn upon exposure to O.

1. Introduction

High Entropy Alloys (HEAs) [1–4] are complex metallic solid solutions with five or more principal elements in non-dilute concentrations that possess superior mechanical and structural properties with respect to conventional metals [5–15]. Besides mechanical properties, the large compositional space of HEAs offers countless possibilities to optimize secondary features, such as biocompatibility [16], corrosion resistance [17], or magnetic behavior [18].

Despite the original focus was primarily on bulk, interest in the surface structure, composition, and reactivity of HEAs recently emerged, triggered by the investigation of the corrosion [17,19,20] and catalytic [21–23] behavior of these alloys. Owing to the vast compositional space of HEAs, the concentration of the elements can be tuned to obtain specific surface structures in order to design corrosion-resistant high performance HEAs, high-entropy coatings for conventional materials (e.g. steels), or highly active, stable, and selective high-entropy catalysts.

A major issue in HEAs is the precipitation of secondary detrimental phases, usually richer in composition of one or more constitutive elements [24–26]. Since element segregation is present in the bulk, even more so it should be observed on surfaces, where segregation energies are usually 10–100 times larger in magnitude. Recent studies however observed a seemingly uniform distribution of elements in high-entropy nanotubes [27], nanoparticles [28–31], and nanoporous structures [32], hinting that surface segregation may be negligible in the investigated HEAs at least in non-reactive conditions. This stands in stark contrast with common bimetallic alloys, such as PtPd, CoCr [33], Ag_3Pd [34], where segregation is commonly reported.

A detailed understanding of the segregation mechanisms in HEAs is of paramount importance for the stability of HEA components [35]: a strong segregation of passivating elements could increase corrosion resistance on one hand, but could compromise the long-term stability of potential high-entropy catalysts on the other. Despite this pivotal role, the degree of surface segregation in HEAs has not been quantified exhaustively in the literature. *Ab initio* simulations of oxidation of a high-entropy alloy were performed for Mo-W-Ta-Ti-Zr [36], but surface segregation was not considered.

In this article, we address the fundamentals of surface segregation for the prototypical Cr-Mn-Fe-Co-Ni HEA [2,37] with first principles calculations. Segregation mechanisms for this alloy are quite controversial: for CrMnFeCoNi, the formation of an external Mn_2O_3 layer and an inner Cr_2O_3 layer upon prolonged exposure to air has been observed [38–40], but very recently Wang et al. [41] found mainly Cr-oxides and hydroxides and Fe-oxides in the native surface layer.

Here we calculate the segregation energies of the component elements of face centered cubic (fcc) Cr-Mn-Fe-Co-Ni as a function of the alloy composition, in vacuum and in the presence of 1 monolayer (ML) of atomic O on the surface. Additionally, we compute formation free energies of various oxides containing the component elements to evaluate the segregation also in the oxide phase. We consider the fcc (111) surface because it is the most close-packed. We show that Ni segregates to the surface in vacuum for Cr-, Mn-, and Fe-rich alloys, whereas Cr and Mn segregate to the surface when O is present for every alloy composition.

In Section 2 we provide the details of the calculation of segregation

* Corresponding author at: Materials Science and Engineering, Delft University of Technology, Mekelweg 2, 2628CD Delft, the Netherlands.
E-mail address: A.Ferrari-1@tudelft.nl (A. Ferrari).

https://doi.org/10.1016/j.apsusc.2020.147471
Received 13 June 2020; Received in revised form 24 July 2020; Accepted 4 August 2020
Available online 11 August 2020
0169-4332/ © 2020 The Author(s). Published by Elsevier B.V. This is an open access article under the CC BY license (http://creativecommons.org/licenses/by/4.0/).

and formation free energies with first-principles calculations and with standard canonical *d*-band models. In Section 3 and 4 we discuss the surface segregation in vacuum and with adsorbed O. In Section 5 we present the formation free energy of different oxides.

2. Calculation of segregation and formation free energies

2.1. Ab initio calculation of the segregation and formation free energies

2.1.1. Segregation free energy

We computed the segregation free energy of an element by comparing the surface free energy of a slab with disordered configurations on the surfaces with that of a slab where the surfaces are fully composed of that element only. Since the disordered and segregated slabs have different number of atoms of each species, we corrected our surface free energies with the chemical potentials of the elements in the Cr-Mn-Fe-Co-Ni alloy. The surface segregation free energy of an element i hence reads [42]

$$G^{(\mathrm{i})}_{\mathrm{segr}} = \frac{1}{N_{\mathrm{s}}}\left[G^{(\mathrm{i})}_{\mathrm{slab}} - G^{(\mathrm{ran})}_{\mathrm{slab}} - \sum_{\mathrm{j}} (n^{(\mathrm{i})}_{\mathrm{j}} - n^{(\mathrm{ran})}_{\mathrm{j}})\mu_{\mathrm{j}} \right], \tag{1}$$

where $G^{(\mathrm{i})}_{\mathrm{slab}}$ and $G^{(\mathrm{ran})}_{\mathrm{slab}}$ are the total free energies of the slabs with the surfaces occupied by element i and by a disordered configuration of the atoms, respectively; N_{s} is the number of atoms on the two surfaces of the slabs; $n^{(\mathrm{i})}_{\mathrm{j}} = N_{\mathrm{s}}\,\delta_{\mathrm{ij}}$ and $n^{(\mathrm{ran})}_{\mathrm{j}}$ are the number of atoms of type j on the surfaces with element i and with the disordered configuration, respectively; and μ_{j} is the chemical potential of the element j.

In the evaluation of the free energies and chemical potentials we have neglected the vibrational, magnetic, and electronic contributions and retained only the configurational part using Stirling's approximation:

$$\begin{aligned} G^{(\mathrm{i})}_{slab} &= E^{(\mathrm{i})}_{slab} \\ G^{(ran)}_{slab} &= E^{(ran)}_{slab} + k_{\mathrm{B}}T \sum_{\mathrm{j}} c_{\mathrm{j}} ln c_{\mathrm{j}}, \end{aligned} \tag{2}$$

where c_{j} indicates the concentration of j in the alloy.

The chemical potential of j is [42]

$$\mu_{\mathrm{j}} = \lim_{c\to 0} \frac{1}{c}[E(\mathrm{A}_{1-c}\mathrm{j}_c) - E(\mathrm{A})] - k_{\mathrm{B}}T\left(\sum_{\mathrm{k}} c_{\mathrm{k}} \ln c_{\mathrm{k}} - \ln c_{\mathrm{j}}\right), \tag{3}$$

where A denotes an alloy with a certain composition (CrMnFeCoNi, for instance). To decrease the computational effort, we did not compute $E(\mathrm{A})$ explicitly, but estimated it via the average of the $E(\mathrm{A}_{1-c}\mathrm{j}_c)$ over the five component elements, i.e.

$$E(\mathrm{A}) = \frac{1}{5}\lim_{c\to 0} \sum_{\mathrm{j}\in\{\mathrm{Cr,Mn,...}\}} E(\mathrm{A}_{1-c}\mathrm{j}_c). \tag{4}$$

Eq. (3) and (4) are exact in the limit $c \to 0$; in practice, we found that utilizing a finite c of about $1-2\%$ introduces negligible errors.

2.1.2. Oxide formation free energies

We computed the formation free energy of an oxide with chemical formula $\mathrm{M_xO_y}$ as

$$G_{\mathrm{form}} = \frac{E(\mathrm{M}_x\mathrm{O}_y) - x\,\mu_{\mathrm{M}} - y\,\mu_{\mathrm{O}}}{x+y}, \tag{5}$$

where

$$\mu_{\mathrm{O}} = \frac{E_{\mathrm{O_2}}}{2} + \frac{E^{(\mathrm{ZPE})}_{\mathrm{O_2}}}{2} + \Delta\mu_{\mathrm{O}}(T,\,p) \tag{6}$$

with $E_{\mathrm{O_2}}$ the total energy of the $\mathrm{O_2}$ molecule, $E^{(\mathrm{ZPE})}_{\mathrm{O_2}}$ the zero-point energy, and $\Delta\mu_{\mathrm{O}}(T,\,p)$ the finite temperature and finite pressure contributions taken from Ref. [43].

2.2. Computational setup

The first principles calculations were performed within the framework of Density Functional Theory (DFT), using the plane-wave projector augmented wave (PAW) method [44,45] as implemented in VASP 5.4 [46–48] and the exact muffin-tin orbital (EMTO) method [49–51].

For the PAW method, we employed the generalized gradient approximation in the PBE parametrization [52]. The 4*s* and 3*d* electrons were treated as valence for Cr, Mn, Fe, Co, and Ni, and the 2*s* and 2*p* electrons for O. The energy cutoff was fixed to 400 eV. The width of the Methfessel-Paxton function [53] for the electronic smearing was 0.1 eV. All the calculations were spin-polarized. The *k*-points sampled the Brillouin zone with Γ-centered Monkhorst–Pack grids [54,55]. We modeled fcc(111) surfaces as $3 \times 3 \times 9$ slabs with 81 atoms with 15 Å of vacuum to separate periodic images and used a *k*-mesh of $4 \times 4 \times 1$. For the calculation of the bulk chemical potentials we considered $3 \times 3 \times 6$ supercells with 54 atoms with the same orientation as the slabs (*z*-direction parallel to [111]) and used a *k*-mesh of $6 \times 6 \times 4$. We relaxed the atomic positions until the interatomic forces decreased to less than 0.05 eV/Å. To minimize artificial ordering due to the finite size of the supercells, we considered 5 different supercell realizations and for each of them 120 different permutations of the positions of the atoms for the calculations of the surface free energies (Eq. (2)) and chemical potentials (Eqs. (3)), respectively. This allowed us to obtain statistical uncertainties of about 40 meV/at. for the segregation free energies.

For the EMTO method, we converged the ground-state electron density using the local density approximation and then calculated the total energy with the generalized gradient approximation from the obtained charge density. We considered the same valence electrons as in the plane-wave pseudopotentials for the component elements. We employed the Fermi smearing with a width of 0.1 eV and obtained our results at the corresponding finite electronic temperature. The *k*-points sampling was performed with the Monkhorst–Pack scheme. We treated the alloys within the coherent potential approximation (CPA) [56,57] with screened Coulomb interactions [58–60]. The screening parameters were obtained with the locally self-consistent Green's function method [61–63] with the same procedure as in Ref. [64]. They take the following values: Cr 0.767, Mn 0.794, Fe 0.316, Co 0.756, Ni 0.804 [65]. Within CPA, we modeled fcc(111) surfaces as 7-layer slabs with roughly 16 Å of vacuum and used a k-mesh of . For the calculation of the chemical potentials we considered fcc unit cells with a k-mesh of $16 \times 16 \times 16$. We performed calculations for the non magnetic (NM), paramagnetic, and ferromagnetic (FM) states. We treated the paramagnetic state with the disordered local moment (DLM) approximation [66,67].

2.3. Canonical relations for the segregation

A qualitative description of the segregation in transition-metal alloys can be obtained also from canonical models exploiting the properties of the *d*-partial density of states (pDOS) and the *d*-band filling, such as the Friedel model and the Hammer-Nørskov model. These models are not quantitatively accurate, but are useful to rationalize important trends with respect to the composition.

2.3.1. Friedel model for the segregation in vacuum

The Friedel model [68] considers a *d*-valent alloy with a rectangular density of states of width w with a band filling f. In this model, the surface segregation energy of another metal, with band filling $f^{\star}$, is related to the difference in the surface formation energies of the two metals [42]:

$$E_{\text{segr}} = \left(1 - \sqrt{\frac{z_s}{z_b}}\right) 5w(f)[f^{\star}(1-f^{\star}) - f(1-f)], \tag{7}$$

where z_s and z_b are the numbers of nearest neighbors for the surface (9 for fcc(111)) and for the bulk (12 for fcc), respectively, and the square-root dependence derives from a second-moment approximation to tight-binding [69].

The average *d*-band filling of Cr-Mn-Fe-Co-Ni is calculated from the number of *d*-electrons of each element. We used the following number of *d*-electrons, found by integrating the pDOS for each metal in the fcc structure up to the Fermi level: Cr 4.3, Mn 5.0, Fe 6.1, Co 7.0, Ni 8.1. For example, the band filling for the equiatomic CrMnFeCoNi is 0.61. Using the computed pDOS, we estimated the bandwidths *w* and parametrized them as a function of *f* (see the Appendix for details).

2.3.2. Hammer-Nørskov model for the segregation with oxygen

Within the Hammer-Nørskov model [70], the binding energy between a metal and an adsorbate species (and consequently also the segregation energy of that metal in the presence of adsorbates) decreases for increasing baricenter of the *d*-band of the metal with respect to its Fermi energy. An extension of the Hammer-Nørskov model to magnetic systems reads [71]

$$E_{\text{segr}} \propto -\frac{\sum_{\sigma} f_{\sigma}\ \epsilon_{d\sigma}}{\sum_{\sigma} f_{\sigma}} - (\epsilon_{d\uparrow} - \epsilon_{d\downarrow})\frac{f_{\uparrow} - f_{\downarrow}}{\sum_{\sigma} f_{\sigma}}, \tag{8}$$

where

$$\epsilon_{d\sigma} = \frac{\int g_{d\sigma}(\epsilon)(\epsilon - \epsilon_F)d\,\epsilon}{\int g_{d\sigma}(\epsilon)d\,\epsilon} \tag{9}$$

are the baricenters of the *d*-band, f_{σ} are the *d*-band fillings and $g_{d\sigma}$ are the pDOS for each spin channel σ.

3. Segregation in vacuum

3.1. The equiatomic CrMnFeCoNi alloy

For the equiatomic CrMnFeCoNi (Cantor) alloy we fixed the lattice parameter to the experimental value of 3.60 Å [2,72–77]. The segregation free energies of Cr, Mn, Fe, Co, and Ni at room temperature in this alloy are presented in Fig. 1. The different bars refer to the PAW and EMTO methods in different magnetic states. The NM segregation free energies are also compared to the Friedel model. The error bars for the PAW method are statistical and due to the finite size of the supercells (see Section 2.2).

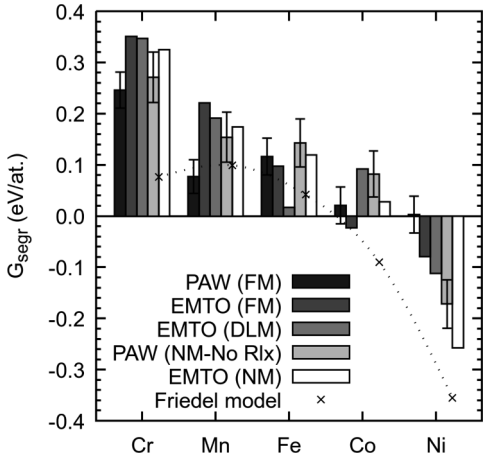

Fig. 1. Segregation free energies at 300 K for the component elements in CrMnFeCoNi calculated with the EMTO method in the ferromagnetic (FM), paramagnetic (DLM), and non-magnetic (NM) states, and with the PAW method in the FM and NM states. For the NM state the atomic positions were not relaxed.

In the NM state, the EMTO method underestimates slightly the segregation free energies of Co and Ni, even if relaxation is not taken into account in the PAW method. The NM segregation energies follow approximately the trend given by the Friedel model. Noteworthy, this simple approximation underestimates the segregation free energies by only roughly 0.15 eV/at.

At fixed atomic positions, magnetism generally increases the segregation energy, with FM having a stronger effect than DLM, but exceptions are found for Fe and Co. The largest impact of magnetism is on Ni, where different magnetic states lead to segregation energies which differ by as much as 0.15 eV/at.

Atomic relaxation has the biggest effect on the segregation energy of Mn, and is accompanied by a relatively large change of the magnetic moment of this element (more than 1 μ_B). This highlights a strong volume-dependence of the magnetic moment of Mn.

We find that the expected segregation of Ni, with the lowest surface formation energy among the five elements, is mitigated by magnetism and configurational entropy. We considered also surface configurations with Co and Ni segregating simultaneously at the surface but did not found substantial differences in segregation energies with respect to the two metals alone. Based on the PAW results in the FM state, we conclude that segregation in CrMnFeCoNi in vacuum at room temperature may be negligible and that the most realistic configuration of the surface at room temperature is likely a Cr-lean solid solution.

The left panel of Fig. 2 displays the magnetic moments of Cr, Mn, Fe, Co, and Ni at different positions in the slabs (on the surface layers, on the subsurface layers, and in bulk-like layers) computed in the FM state with the PAW and EMTO methods. The most notable difference between the two methods is the ferromagnetic alignment of Mn in the subsurface layer for the EMTO method; we observed this ferromagnetic alignment also in the PAW method with unrelaxed atomic positions, but it disappeared when atomic positions were relaxed; this is imputed to the already mentioned strong dependence of the magnetic moment of Mn on interatomic distances. The magnetic moments converge approximately to the bulk value already from the second layer below the surface for all component elements. The right panel of Fig. 2 shows the magnitude of the converged magnetic moments in the DLM state obtained with the EMTO method as a function of the position in the slab. In the bulk at the experimental volume and in the idealized DLM state, only for Mn and Fe finite local magnetic moments are observed in agreement with previous reports [37]. The inclusion of longitudinal spin fluctuations in other works stabilized the local magnetic moments in the DLM state [64,78] in the bulk. These details are however beyond the scope of the present work.

3.2. Off-equiatomic compositions

As Ni is the element most prone to segregation in vacuum, we calculated the segregation energy of this element for other compositions. We also tested Co, but found that its segregation energy is always higher than that of Ni.

For the PAW method we considered additional systems with stoichiometry $A_{40}B_{15}C_{15}D_{15}E_{15}$. For the EMTO method we studied all quinary compositions with at least 10% of each element with increasing/decreasing concentration steps of 10% (e.g. $A_{60}B_{10}C_{10}D_{10}E_{10}$, $A_{50}B_{20}C_{10}D_{10}E_{10}$, $A_{40}B_{20}C_{20}D_{10}E_{10}$, etc.). In addition, we considered quaternary, ternary, and binary Cr- and Ni-rich alloys with Cr and Ni concentrations up to 90% to span two corners of the compositional space. For each system we computed the equilibrium volume via a Birch-Murnaghan fit [79,80] of the equation of state.

The segregation energies of Ni at 0 K for the various Cr-Mn-Fe-Co-Ni alloys are reported in Fig. 3 as a function of the *d*-band filling for the PAW and EMTO methods and for the Friedel model.

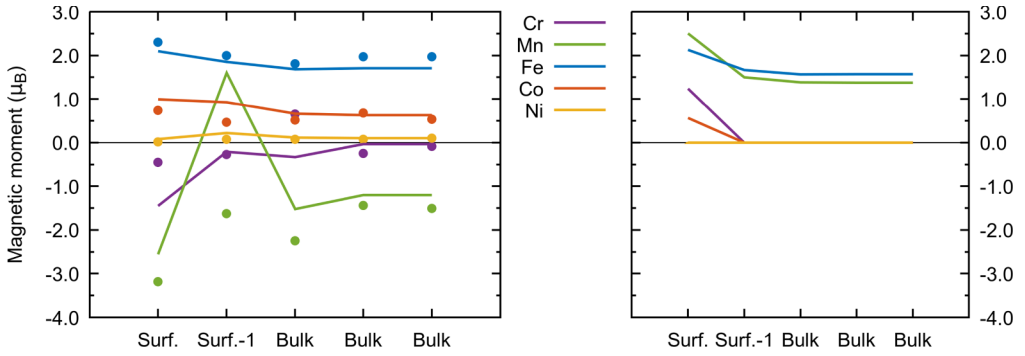

Fig. 2. Converged magnetic moments as a function of position in the slab for the component elements computed with the PAW method (points) and the EMTO method (lines) in the FM state (left panel) and paramagnetic (DLM) state (right panel, only absolute values of the moments calculated with the EMTO method).

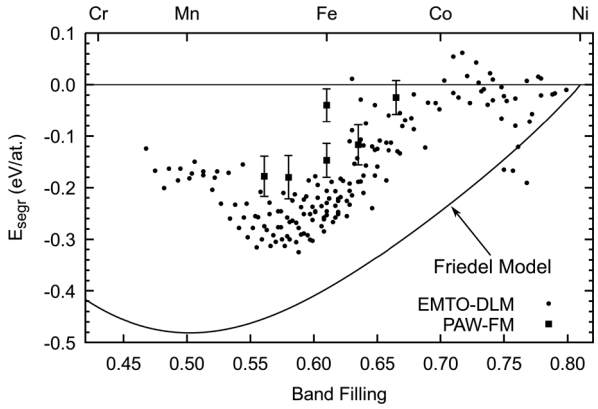

Fig. 3. Segregation energies at 0 K of Ni for Cr-Mn-Fe-Co-Ni as a function of the band filling calculated with the EMTO method in the paramagnetic state (EMTO-DLM), with the PAW method in the ferromagnetic state (VASP-FM), and with the Friedel model.

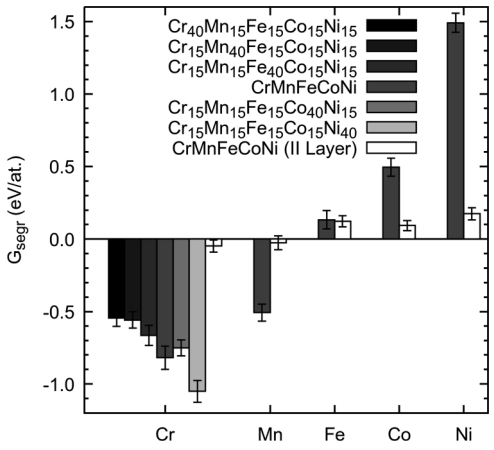

Fig. 4. Segregation free energies at 300 K for the component elements in Cr-Mn-Fe-Co-Ni in the presence of 1 ML of O. For the equiatomic composition the segregation energies in the subsurface layer, provided that the surface layer is fully occupied by Cr, are displayed as well.

When comparing the PAW with the EMTO method and the Friedel model, a similar picture to the segregation in CrMnFeCoNi emerges: the EMTO method and the Friedel model underestimate the segregation energy of Ni, the Friedel model performing again surprisingly well.

The three series of data highlight a clear band filling effect, with the segregation energy of Ni reaching a minimum for a band filling of 0.50–0.55, corresponding to Cr- and Mn-rich alloys, and approaching zero for Ni-rich alloys. The equiatomic CrMnFeCoNi alloy described in the previous Section is apparently an outlier for the PAW data points. This highlights a particularly stable configuration of the random surface and bulk (relatively low chemical potential of Ni) for the equiatomic composition.

We argue in general that segregation is negligible for $f > 0.65$ (Co- and Ni-rich alloys) even at low temperature, whereas there is a weak (E_{segr} ranges from -0.2 to -0.1 eV/at.) segregation of Ni (and Co) at lower band fillings (apart from the equiatomic composition).

4. Segregation with an oxygen layer

To evaluate the impact of reactants on the surface, we analyzed the segregation in the presence of 1 ML of O adsorbed in the fcc hollow positions. For this we employed the PAW method for the equiatomic CrMnFeCoNi alloy as well as for prototypical off-stoichiometric compositions $A_{40}B_{15}C_{15}D_{15}E_{15}$ enriched in A.

Fig. 4 presents the segregation free energies of the elements in the presence of adsorbed O. The picture changes substantially with respect to the bare surface: the binding of O promotes a strong segregation of Cr and Mn at all compositions, whereas Co and Ni tend to strongly antisegregate. The segregation energies for the five elements follow again a clear *d*-band filling effect, the elements with a lower band filling occupying more favorably the surface sites. This follows the predictions of the Hammer-Nørskov model: as shown in Fig. 5 the segregation energies for CrMnFeCoNi correlate very well with the adsorption energies of O on the pure elements (blue squares) and with the baricenter of the *d*-band (red circles) calculated as in Eq. (8).

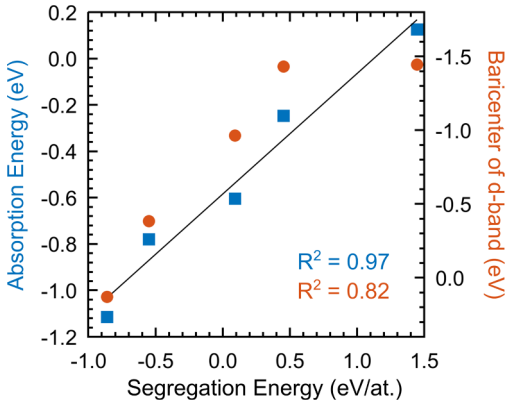

Fig. 5. Correlation between the segregation energy of the component elements in CrMnFeCoNi, the absorption energy of O on the pure component elements, and the baricenter of the *d*-band.

If the composition of the alloy is changed, the segregation energy of

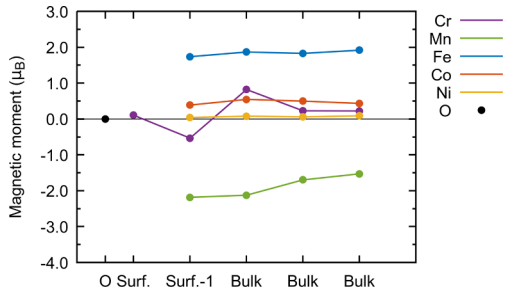

Fig. 6. Converged magnetic moments as a function of position in the slab for the component elements computed with the PAW method in the FM state. The surface layer contains only Cr atoms and is covered by 1 ML of O.

Cr generally decreases with increasing *d*-band filling. The exact magnitude of the segregation energy depends though on the specific Cr content (that affects strongly the chemical potential) and band-filling arguments do not hold strictly: for example, the segregation energy of Cr in CrMnFeCoNi ($f = 0.610$) is lower than that in $Cr_{15}Mn_{15}Fe_{15}Co_{40}Ni_{15}$ ($f = 0.635$).

Given that the strongest segregating element is Cr, we also studied the segregation in the subsurface layer if the surface layer is fully occupied by this element. The results are plotted as white bars in Fig. 4. It can be seen that Cr tends to segregate also to the subsurface layer, but much more weakly.

The magnetic moments of the most stable surface configuration with adsorbed O are displayed in Fig. 6. The O and Cr atoms on the surface have negligible magnetic moment. The moments of the atoms on the other layers do not differ substantially from those with a clean surface, apart from the lower magnetic moment of Mn in the subsurface layer.

5. Segregation in the oxide phase

To investigate the preference towards oxide formation for the various elements, which impacts the segregation in the presence of O, we computed the formation free energies of various metal-oxides. We shortlisted the structures by selecting all the stoichiometries within 40 meV/at. from the 0 K convex hull taken from the Materials Project [81,82]. For each oxide, we relaxed the atomic degrees of freedom, the shape, and the volume of the simulation cells. We found some minor discrepancies in comparing our formation energies with those from the Materials Project, where the Hubbard U parameter was introduced to correct the spurious self-interaction. These discrepancies regarded mainly the equiatomic oxides (MnO, FeO, CoO, and NiO) but have no impact on our conclusions.

The formation free energies of the candidate oxides at 300 K are shown in Fig. 7. To calculate the chemical potential of O, we fixed the partial pressure of this element to 0.2 atm. In these conditions, the formation of oxides is strongly exothermic for all the considered compounds. According to our predictions, the most stable oxide is Cr_2O_3 and this points to the segregation of Cr also in the oxide phase. The trend of the oxide formation energies is the same as that of the segregation energy in the presence of oxygen: the elements with lower band filling, Cr and Mn, have a higher affinity to O than the other elements, especially Ni. The situation does not change substantially for off-equiatomic compositions ($A_{40}B_{15}C_{15}D_{15}E_{15}$), with different chemical potentials.

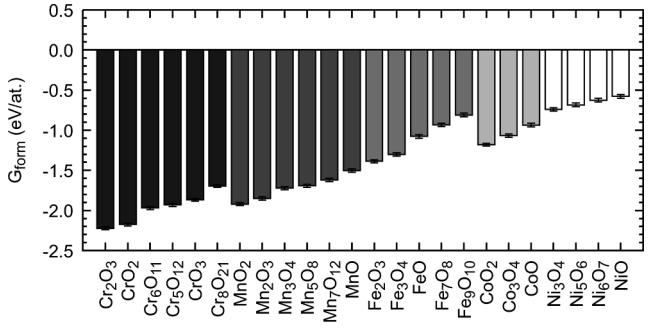

Fig. 7. Formation free energies of oxides at 300 K with $p_{O_2} = 0.2$ atm computed with the PAW method.

A Cr-enrichment has been observed by Wang et al. [41] in the oxide phase of CrMnFeCoNi, in agreement with our findings. Other studies [38–40] reported the formation of an external Mn_2O_3 layer and an internal Cr_2O_3 layer. We impute this discrepancy to the very slow diffusion of Cr in the bulk [25] and oxide [39] phases, that hinders the formation of the thermodynamically most stable oxide (Cr_2O_3) in favor of other metastable phases.

6. Conclusions

Surface segregation in HEAs is not conceptually different from conventional alloys and segregation patterns follow in general the canonical relations (Friedel model, Hammer-Nørskov model). However, magnetism and configurational entropy counteract chemical driving forces and in some cases segregation is prevented even at low temperature.

For Cr-Mn-Fe-Co-Ni in vacuum we found a weak segregation of Ni at low band filling ($f < 0.60$) and negligible segregation at high band filling ($f > 0.65$). In the presence of O, Cr and Mn segregate strongly on the surface and also in the oxide phase.

From a materials design perspective, it must therefore be considered that the composition of the surface of Cr-Mn-Fe-Co-Ni alloys may differ from that of the bulk for Cr-, Mn-, or Fe-rich alloys, or in the presence of reactants on the surface.

In general, surface segregation in HEAs is in most cases not negligible. This could turn out to be an issue or a desirable property, depending on the target application, for instance catalysis or corrosion. The utilized methodology and approach can be straightforwardly applied to other alloys, such as noble-element HEAs or refractory HEAs. For these alloy classes the canonical models may even work better due to the suppression of magnetic effects.

7. CRediT authorship contribution statement

Alberto Ferrari: Conceptualization, Methodology, Validation, Formal analysis, Investigation, Data curation, Writing - original draft, Funding acquisition. **Fritz Körmann:** Conceptualization, Methodology, Software, Resources, Writing - review & editing, Supervision, Project administration, Funding acquisition.

Declaration of Competing Interest

The authors declare that they have no known competing financial interests or personal relationships that could have appeared to influence the work reported in this paper.

Acknowledgements

This work was supported by the Ruhr University Research School PLUS, funded by Germany's Excellence Initiative [DFG GSC 98/3]. The authors thank Andrei Ruban for the very generous help with the EMTO program, Yuji Ikeda for providing the structures for the calculation of the bulk chemical potential, and Mira Todorova, Marcel Sluiter, and Jörg Neugebauer for inspiring discussions.

Appendix A. Parametrization of the bandwidth in the Friedel model

The d-bandwidth was estimated from the pDOS calculated with the EMTO method for each considered alloy composition in the non-magnetic state. To obtain a handy expression, we parametrized it as a function of the band filling f and the unitary cell volume V as

$$w(f, V) = 39.430 - 56.552f - 2.6754V + 4.7065fV, \quad \text{(A.1)}$$

where w is in eV and V in Å^3. This parametrization guarantees a root-mean-squared (rms) error of only 33 meV on w.

The volume V can be further expressed in terms of the band filling via the following expansion of the fcc lattice parameter a (in Å):

$$a(f) = -0.47088 + 0.36351f + 502.26f^2, \quad \text{(A.2)}$$

with a rms error of 0.012 Å.

References

[1] J.-W. Yeh, S.-K. Chen, S.-J. Lin, J.-Y. Gan, T.-S. Chin, T.-T. Shun, C.-H. Tsau, S.-Y. Chang, Nanostructured high-entropy alloys with multiple principal elements: novel alloy design concepts and outcomes, Adv. Eng. Mater. 6 (2004) 299–303.
[2] B. Cantor, I. Chang, P. Knight, A. Vincent, Microstructural development in equiatomic multicomponent alloys, Mater. Sci. Eng. A 375 (2004) 213–218.
[3] B.S. Murty, J.-W. Yeh, S. Ranganathan, P. Bhattacharjee, High-entropy Alloys, Elsevier, 2019.
[4] Y. Ikeda, B. Grabowski, F. Körmann, Ab initio phase stabilities and mechanical properties of multicomponent alloys: a comprehensive review for high entropy alloys and compositionally complex alloys, Mater. Charact. 147 (2019) 464–511.
[5] O.N. Senkov, G. Wilks, J. Scott, D.B. Miracle, Mechanical properties of $Nb_{25}Mo_{25}Ta_{25}W_{25}$ and $V_{20}Nb_{20}Mo_{20}Ta_{20}W_{20}$ refractory high entropy alloys, Intermetallics 19 (2011) 698–706.
[6] A. Gali, E.P. George, Tensile properties of high-and medium-entropy alloys, Intermetallics 39 (2013) 74–78.
[7] F. Otto, A. Dlouhý, C. Somsen, H. Bei, G. Eggeler, E.P. George, The influences of temperature and microstructure on the tensile properties of a CoCrFeMnNi high-entropy alloy, Acta Mater. 61 (2013) 5743–5755.
[8] B. Gludovatz, A. Hohenwarter, D. Catoor, E.H. Chang, E.P. George, R.O. Ritchie, A fracture-resistant high-entropy alloy for cryogenic applications, Science 345 (2014) 1153–1158.
[9] D.B. Miracle, J.D. Miller, O.N. Senkov, C. Woodward, M.D. Uchic, J. Tiley, Exploration and development of high entropy alloys for structural applications, Entropy 16 (2014) 494–525.
[10] Y. Zhang, T.T. Zuo, Z. Tang, M.C. Gao, K.A. Dahmen, P.K. Liaw, Z.P. Lu, Microstructures and properties of high-entropy alloys, Progr. Mater. Sci. 61 (2014) 1–93.
[11] B. Gludovatz, E.P. George, R.O. Ritchie, Processing, microstructure and mechanical properties of the CrMnFeCoNi high-entropy alloy, JOM 67 (2015) 2262–2270.
[12] D.B. Miracle, O.N. Senkov, A critical review of high entropy alloys and related concepts, Acta Mater. 122 (2017) 448–511.
[13] P. Sarker, T. Harrington, C. Toher, C. Oses, M. Samiee, J.-P. Maria, D.W. Brenner, K.S. Vecchio, S. Curtarolo, High-entropy high-hardness metal carbides discovered by entropy descriptors, Nat. Commun. 9 (2018) 1–10.
[14] Y. Ikeda, F. Körmann, I. Tanaka, J. Neugebauer, Impact of chemical fluctuations on stacking fault energies of CrCoNi and CrMnFeCoNi high entropy alloys from first principles, Entropy 20 (2018) 655.
[15] Y. Ikeda, I. Tanaka, J. Neugebauer, F. Körmann, Impact of interstitial C on phase stability and stacking-fault energy of the CrMnFeCoNi high-entropy alloy, Phys. Rev. Mater. 3 (2019) 113603.
[16] W.-Y. Ching, S. San, J. Brechtl, R. Sakidja, M. Zhang, P.K. Liaw, Fundamental electronic structure and multiatomic bonding in 13 biocompatible high-entropy alloys, npj Comput. Mater. 6 (2020) 1–10.
[17] Y. Chou, J. Yeh, H. Shih, The effect of molybdenum on the corrosion behaviour of the high-entropy alloys $Co_{1.5}CrFeNi_{1.5}Ti_{0.5}Mo_x$ in aqueous environments, Corros. Sci. 52 (2010) 2571–2581.
[18] C. Chen, H. Zhang, Y. Fan, W. Zhang, R. Wei, T. Wang, T. Zhang, F. Li, A novel ultrafine-grained high entropy alloy with excellent combination of mechanical and soft magnetic properties, J. Magn. Magn. Mater. 502 (2020) 166513.
[19] Y. Shi, B. Yang, P.K. Liaw, Corrosion-resistant high-entropy alloys: a review, Metals 7 (2017) 43.
[20] Y. Qiu, S. Thomas, M.A. Gibson, H.L. Fraser, N. Birbilis, Corrosion of high entropy alloys, npj Mater. Degrad. 1 (2017) 1–18.
[21] T.A. Batchelor, J.K. Pedersen, S.H. Winther, I.E. Castelli, K.W. Jacobsen, J. Rossmeisl, High-entropy alloys as a discovery platform for electrocatalysis, Joule 3 (2019) 834–845.
[22] T. Löffler, A. Savan, A. Garzón-Manjón, M. Meischein, C. Scheu, A. Ludwig, W. Schuhmann, Toward a paradigm shift in electrocatalysis using complex solid solution nanoparticles, ACS Energy Lett. 4 (2019) 1206–1214.
[23] T. Löffler, A. Savan, H. Meyer, M. Meischein, V. Strotkötter, A. Ludwig, W. Schuhmann, Design von komplexen Mischkristall-Elektrokatalysatoren auf Basis der Korrelation von Konfiguration, Verteilungsmustern der Adsorptionsenergie und Aktivitätskurven, Angew. Chem. 132 (2020) 5893–5900.
[24] F. Otto, A. Dlouhý, K.G. Pradeep, M. Kuběnová, D. Raabe, G. Eggeler, E.P. George, Decomposition of the single-phase high-entropy alloy CrMnFeCoNi after prolonged anneals at intermediate temperatures, Acta Mater. 112 (2016) 40–52.
[25] K.-Y. Tsai, M.-H. Tsai, J.-W. Yeh, Sluggish diffusion in Co–Cr–Fe–Mn–Ni high-entropy alloys, Acta Mater. 61 (2013) 4887–4897.
[26] Y. Wang, M. Yan, Q. Zhu, W.Y. Wang, Y. Wu, X. Hui, R. Otis, S.-L. Shang, Z.-K. Liu, L.-Q. Chen, Computation of entropies and phase equilibria in refractory V-Nb-Mo-Ta-W high-entropy alloys, Acta Mater. 143 (2018) 88–101.
[27] A.-L. Wang, H.-C. Wan, H. Xu, Y.-X. Tong, G.-R. Li, Quinary PdNiCoCuFe alloy nanotube arrays as efficient electrocatalysts for methanol oxidation, Electrochim. Acta 127 (2014) 448–453.
[28] Y. Yao, Z. Huang, P. Xie, S.D. Lacey, R.J. Jacob, H. Xie, F. Chen, A. Nie, T. Pu, M. Rehwoldt, et al., Carbothermal shock synthesis of high-entropy-alloy nanoparticles, Science 359 (2018) 1489–1494.
[29] T. Löffler, H. Meyer, A. Savan, P. Wilde, A. Garzón Manjón, Y.-T. Chen, E. Ventosa, C. Scheu, A. Ludwig, W. Schuhmann, Discovery of a multinary noble metal–free oxygen reduction catalyst, Adv. Energy Mater. 8 (2018) 1802269.
[30] M.W. Glasscott, A.D. Pendergast, S. Goines, A.R. Bishop, A.T. Hoang, C. Renault, J.E. Dick, Electrosynthesis of high-entropy metallic glass nanoparticles for designer, multi-functional electrocatalysis, Nat. Commun. 10 (2019) 1–8.
[31] P. Xie, Y. Yao, Z. Huang, Z. Liu, J. Zhang, T. Li, G. Wang, R. Shahbazian-Yassar, L. Hu, C. Wang, Highly efficient decomposition of ammonia using high-entropy alloy catalysts, Nat. Commun. 10 (2019) 1–12.
[32] H.-J. Qiu, G. Fang, Y. Wen, P. Liu, G. Xie, X. Liu, S. Sun, Nanoporous high-entropy alloys for highly stable and efficient catalysts, J. Mater. Chem. A 7 (2019) 6499–6506.
[33] A. Dianat, J. Zimmermann, N. Seriani, M. Bobeth, W. Pompe, L.C. Ciacchi, Ab initio study of element segregation and oxygen adsorption on PtPd and CoCr binary alloy surfaces, Surf. Sci. 602 (2008) 876–884.
[34] J.R. Kitchin, K. Reuter, M. Scheffler, Alloy surface segregation in reactive environments: first-principles atomistic thermodynamics study of Ag_3Pd (111) in oxygen atmospheres, Phys. Rev. B 77 (2008) 075437.
[35] S.D. Lacey, Q. Dong, Z. Huang, J. Luo, H. Xie, Z. Lin, D.J. Kirsch, V. Vattipalli, C. Povinelli, W. Fan, et al., Stable multimetallic nanoparticles for oxygen electrocatalysis, Nano Lett. 19 (2019) 5149–5158.
[36] E. Osei-Agyemang, G. Balasubramanian, Surface oxidation mechanism of a refractory high-entropy alloy, npj Mater, Degrad. 3 (2019) 1–8.
[37] D. Ma, B. Grabowski, F. Körmann, J. Neugebauer, D. Raabe, Ab initio thermodynamics of the CoCrFeMnNi high entropy alloy: Importance of entropy contributions beyond the configurational one, Acta Mater. 100 (2015) 90–97.
[38] G.R. Holcomb, J. Tylczak, C. Carney, Oxidation of CoCrFeMnNi high entropy alloys, JOM 67 (2015) 2326–2339.
[39] G. Laplanche, U. Volkert, G. Eggeler, E. George, Oxidation behavior of the CrMnFeCoNi high-entropy alloy, Oxid. Met. 85 (2016) 629–645.
[40] Y. Li, A. Savan, A. Kostka, H. Stein, A. Ludwig, Accelerated atomic-scale exploration of phase evolution in compositionally complex materials, Mater. Horiz. 5 (2018) 86–92.
[41] L. Wang, D. Mercier, S. Zanna, A. Seyeux, M. Laurent-Brocq, L. Perriere, I. Guillot, P. Marcus, Study of the surface oxides and corrosion behaviour of an equiatomic CoCrFeMnNi high entropy alloy by XPS and ToF-SIMS, Corros. Sci. 108507 (2020).
[42] A. Ruban, H.L. Skriver, J.K. Nørskov, Surface segregation energies in transition-metal alloys, Phys. Rev. B 59 (1999) 15990.
[43] J. Rogal, K. Reuter, Ab Initio Atomistic Thermodynamics for Surfaces: A Primer, Technical Report, Max-Planck-Gesellschaft zur Förderung der Wissenschaften e.V, Berlin (Germany), 2006.
[44] P.E. Blöchl, Projector augmented-wave method, Phys. Rev. B 50 (1994) 17953.
[45] G. Kresse, D. Joubert, From ultrasoft pseudopotentials to the projector augmented-wave method, Phys. Rev. B 59 (1999) 1758.
[46] G. Kresse, J. Hafner, Ab initio molecular dynamics for liquid metals, Phys. Rev. B 47 (1993) 558.
[47] G. Kresse, J. Furthmüller, Efficiency of ab-initio total energy calculations for metals and semiconductors using a plane-wave basis set, Comput. Mater. Sci. 6 (1996) 15–50.
[48] G. Kresse, J. Furthmüller, Efficient iterative schemes for ab initio total-energy calculations using a plane-wave basis set, Phys. Rev. B 54 (1996) 11169.
[49] L. Vitos, H.L. Skriver, B. Johansson, J. Kollár, Application of the exact muffin-tin orbitals theory: the spherical cell approximation, Comput. Mater. Sci. 18 (2000) 24–38.
[50] L. Vitos, Total-energy method based on the exact muffin-tin orbitals theory, Phys. Rev. B 64 (2001) 014107.
[51] L. Vitos, Computational Quantum Mechanics for Materials Engineers: the EMTO Method and Applications, Springer Science & Business Media, 2007.

[52] J.P. Perdew, K. Burke, M. Ernzerhof, Generalized gradient approximation made simple, Phys. Rev. Lett. 77 (1996) 3865.
[53] M. Methfessel, A. Paxton, High-precision sampling for brillouin-zone integration in metals, Phys. Rev. B 40 (1989) 3616.
[54] A. Baldereschi, Mean-value point in the brillouin zone, Phys. Rev. B 7 (1973) 5212.
[55] H.J. Monkhorst, J.D. Pack, Special points for brillouin-zone integrations, Phys. Rev. B 13 (1976) 5188.
[56] P. Soven, Coherent-potential model of substitutional disordered alloys, Phys. Rev. 156 (1967) 809.
[57] B. Gyorffy, Coherent-potential approximation for a nonoverlapping-muffin-tin-potential model of random substitutional alloys, Phys. Rev. B 5 (1972) 2382.
[58] A.V. Ruban, H.L. Skriver, Screened coulomb interactions in metallic alloys. i. Universal screening in the atomic-sphere approximation, Phys. Rev. B 66 (2002) 024201.
[59] A.V. Ruban, S. Simak, P.A. Korzhavyi, H.L. Skriver, Screened coulomb interactions in metallic alloys. ii. Screening beyond the single-site and atomic-sphere approximations, Phys. Rev. B 66 (2002) 024202.
[60] J. Faulkner, Y. Wang, G. Stocks, Electrons in extended systems, Phys. Rev. B 52 (1995) 17106.
[61] I. Abrikosov, A. Niklasson, S. Simak, B. Johansson, A. Ruban, H.L. Skriver, Order-n Green's function technique for local environment effects in alloys, Phys. Rev. Lett. 76 (1996) 4203.
[62] I. Abrikosov, S. Simak, B. Johansson, A. Ruban, H.L. Skriver, Locally self-consistent Green's function approach to the electronic structure problem, Phys. Rev. B 56 (1997) 9319.
[63] O.E. Peil, A.V. Ruban, B. Johansson, Self-consistent supercell approach to alloys with local environment effects, Phys. Rev. B 85 (2012) 165140.
[64] B. Schönfeld, C.R. Sax, J. Zemp, M. Engelke, P. Boesecke, T. Kresse, T. Boll, T. Al-Kassab, O.E. Peil, A.V. Ruban, Local order in Cr-Fe-Co-Ni: experiment and electronic structure calculations, Phys. Rev. B 99 (2019) 014206.
[65] A.V. Ruban, Private correspondence, 2020.
[66] J. Staunton, B. Gyorffy, A. Pindor, G. Stocks, H. Winter, The "disordered local moment" picture of itinerant magnetism at finite temperatures, J. Magn. Magn. Mater. 45 (1984) 15–22.
[67] B. Gyorffy, A. Pindor, J. Staunton, G. Stocks, H. Winter, A first-principles theory of ferromagnetic phase transitions in metals, J. Phys. F 15 (1985) 1337.
[68] A.P. Sutton, Electronic Structure of Materials, Clarendon Press, 1993.
[69] F. Cyrot-Lackmann, On the electronic structure of liquid transitional metals, Adv. Phys. 16 (1967) 393–400.
[70] B. Hammer, J. Nørskov, Electronic factors determining the reactivity of metal surfaces, Surf. Sci. 343 (1995) 211–220.
[71] S. Bhattacharjee, U.V. Waghmare, S.-C. Lee, An improved d-band model of the catalytic activity of magnetic transition metal surfaces, Sci. Rep. 6 (2016) 35916.
[72] P. Bhattacharjee, G. Sathiaraj, M. Zaid, J. Gatti, C. Lee, C.-W. Tsai, J.-W. Yeh, Microstructure and texture evolution during annealing of equiatomic CoCrFeMnNi high-entropy alloy, J. Alloy Compd. 587 (2014) 544–552.
[73] Z. Wu, Temperature and alloying effects on the mechanical properties of equiatomic FCC solid solution alloys, Ph.D. thesis University of Tennessee, 2014.
[74] M. Laurent-Brocq, A. Akhatova, L. Perrière, S. Chebini, X. Sauvage, E. Leroy, Y. Champion, Insights into the phase diagram of the CrMnFeCoNi high entropy alloy, Acta Mater. 88 (2015) 355–365.
[75] B. Schuh, F. Mendez-Martin, B. Völker, E.P. George, H. Clemens, R. Pippan, A. Hohenwarter, Mechanical properties, microstructure and thermal stability of a nanocrystalline CoCrFeMnNi high-entropy alloy after severe plastic deformation, Acta Mater. 96 (2015) 258–268.
[76] C.L. Tracy, S. Park, D.R. Rittman, S.J. Zinkle, H. Bei, M. Lang, R.C. Ewing, W.L. Mao, High pressure synthesis of a hexagonal close-packed phase of the high-entropy alloy CrMnFeCoNi, Nat. Commun. 8 (2017) 1–6.
[77] F. Zhang, Y. Wu, H. Lou, Z. Zeng, V.B. Prakapenka, E. Greenberg, Y. Ren, J. Yan, J.S. Okasinski, X. Liu, et al., Polymorphism in a high-entropy alloy, Nat. Commun. 8 (2017) 1–7.
[78] Z. Dong, L. Vitos, Finite temperature magnetic properties of $Cr_xCo_yNi_{100-x-y}$ medium entropy alloys from first principles, Scripta Mater. 171 (2019) 78–82.
[79] F. Murnaghan, The compressibility of media under extreme pressures, PNAS 30 (1944) 244.
[80] F. Birch, Finite elastic strain of cubic crystals, Phys. Rev. 71 (1947) 809.
[81] A. Jain, S.P. Ong, G. Hautier, W. Chen, W.D. Richards, S. Dacek, S. Cholia, D. Gunter, D. Skinner, G. Ceder, et al., Commentary: The materials project: A materials genome approach to accelerating materials innovation, APL Mater. 1 (2013) 011002.
[82] A. Jain, G. Hautier, S.P. Ong, C.J. Moore, C.C. Fischer, K.A. Persson, G. Ceder, Formation enthalpies by mixing GGA and GGA + U calculations, Phys. Rev. B 84 (2011) 045115.